Chemical Science

Accepted Manuscript

This article can be cited before page numbers have been issued, to do this please use: D. Yu, B. Liu, D. Li, J. Yu, X. Lan, S. Liu, Z. Li, P. Gao, Y. Zhang and H. Zhao, *Chem. Sci.*, 2026, DOI: 10.1039/D6SC01575A.

ROYAL SOCIETY OF CHEMISTRY

rsc.li/chemical-science

View Article Online
DOI: 10.1039/D6SC01575A

ARTICLE

ZrO_2 induced *d*–*d* spatial coordination effects of Ru single-atom catalysts to boost oxygen evolution reaction

Received 00th January 20xx,
Accepted 00th January 20xx

DOI: 10.1039/x0xx00000x

Dandan Yu,[a] Bin Liu, [a] Dongming Li, [a] Junkai Yu, [a] Xijie Lan, [a] Shuhong Liu, [a] Zhuxin Li, [b] Pengyun Gao, [b] Yong Zhang*[a] and Hong Zhao*[b]

Proton exchange membrane water electrolysis (PEMWE) is a leading strategy for producing green hydrogen from intermittent renewable energy. However, the high anodic energy barrier of the oxygen evolution reaction (OER), in strongly acidic and highly oxidative operating environment, poses severe challenges for catalyst design. Herein, based on a unique *d*–*d* spatial coordination design, tetragonal zirconia supported Ru single-atom catalysts (Ru-RSZ) were synthesized, which exhibited an overpotential as low as 208 mV and a mass activity of 1452.61 A·g_{Ru}^{-1} @1.51V. Remarkably, these catalysts were stably operated for 500 h. X-ray absorption spectroscopy (XAS) and high-angle annular dark-field (HAADF) demonstrated that Ru is atomically dispersed at Zr lattice sites in ZrO_2, and the point-group symmetry of the Ru atom changes from D_{2h} in RuO_2 to D_{2d}. Density functional theory (DFT) calculations elucidated that the *d*-band center of Ru atoms was lowered by *d*–*d* spatial coordination effects, which weakened the strong adsorption of oxygen at Ru sites, eventually reducing the activation barrier of the OER rate-determining step. This work paves a new avenue to design high-efficient and stable catalysts for hydrogen production fields.

Introduction

Against the backdrop of advancing green, low-carbon development and the global energy transition, hydrogen production from water electrolysis has emerged as a cornerstone technology for building the future energy system.[1-4] Proton exchange membrane water electrolysis (PEMWE) has garnered significant attention due to its higher current density, rapid kinetics and higher stack efficiency (70—77 %) in contrast to alkaline water electrolysis.[5,6] However, the oxygen evolution reaction (OER) of PEMWE systems involves complex multi-step proton-coupled electron transfer processes and demonstrates sluggish kinetics, which significantly limit the overall efficiency of water electrolysis.[7,8] Furthermore, protonation and solvation effects in acidic media pose substantial challenges to the stability of anode catalysts.[9] Currently, only iridium-based oxides are widely used as OER catalysts, but the high-cost and scarcity disadvantages severely limit their large-scale applications.[10,11] To address these challenges, extensive research has focused on finding alternative catalysts, with cost-effective (10 times cheaper than iridium)[12] and Earth-abundant[13] ruthenium (Ru) emerging as a promising iridium substitute owing to its comparable catalytic activity.[14-16] Nevertheless, the durability of ruthenium oxides remains limited and insufficient to meet the long-term operational requirements of commercial-scale PEMWE systems.[17] Moreover, as a noble metal, ruthenium still entails substantial cost.[18] To satisfy the commercial demands of PEMWE for industrial hydrogen production, it is imperative to develop low-cost Ru electrocatalysts with high-activity and long-term stability.

Nowadays, the development of Ru-based electrocatalysts primarily encompass doping and defect engineering, interface engineering, and hybridized orbitals engineering etc.[16,19,20] Among these, orbital coupling between RuO_2 and heteroatom dopants has demonstrated pronounced enhancement and stabilization of active sites.[21] For example, Pb doping produces Pb–O–Ru 6*s*–2*p*–4*d* orbital hybridization that increases the energy required to remove lattice oxygen, thereby suppressing excessive oxidation of Ru.[22] Similarly, unique lanthanide dopants induce *f*–*p*–*d* gradient orbital coupling that can modify adsorption energies of reaction intermediates and inhibit involvement of lattice oxygen, thus preventing over-oxidation of Ru.[23] However, Ru–M orbital coupling mediated by O bridges is weakened by the presence of O 2*p* orbitals. Moreover, studies of dopant-induced orbital coupling based on the rutile structure have frequently neglected the strong influence of local atomic coordination, although some works have compared OER performance of Ru located at sites of different symmetries in other structures such as pyrochlore,[24] perovskites,[25,26] investigations specifically addressing how crystal-structure-driven differences alter orbital coupling remain scarce. More importantly, substantial amounts of Ru catalysts are still required in doped RuO_2 systems, which is not satisfied with the low-cost requirement of industrial hydrogen production.

In this work, acid-resistant oxide ZrO_2 was adopted as the support to provide Ru atoms with a distinctive atomic

[a] School of Materials Science and Engineering, Dalian Jiaotong University, Dalian 116028, China. E-mail: zhangyong0411@126.com
[b] College of Material Science and Engineering, Sichuan University of Science & Engineering, Zigong 643000, China. E-mail: zhaohong@suse.edu.cn

View Article Online
DOI: 10.1039/D6SC01575A

coordination geometry ($P4_2/nmc$).[27] A Ru single-atom catalyst supported on ZrO_2 (Ru-RSZ) was synthesized via a hydrothermal method. X-ray diffraction (XRD) and Raman characterization indicate that introduction of Ru stabilizes the tetragonal phase of ZrO_2. Further high-angle annular dark-field scanning transmission electron microscopy (HAADF-STEM) and X-ray absorption spectroscopy (XAS) analyses reveal that Ru occupies Zr lattice sites, with site symmetry transformed from D_{2h} in RuO_2 to D_{2d} in ZrO_2. Density functional theory (DFT) calculations reveal that the unique *d*–*d* interactions in Ru-RSZ furnish direct bonding, substantially lowering the Ru 4*d*-band center, suppressing strong adsorption of oxygen intermediates on Ru, reducing reaction barriers, and concurrently weakening Ru–O covalency to inhibit participation of lattice oxygen, thereby enhancing structural stability. The synthesized Ru-RSZ catalyst exhibits an overpotential reduced to 208 mV at a Ru loading of only 43.9 $\mu g_{Ru} \cdot cm^{-2}$, and chronopotentiometry at a current density of 10 $mA \cdot cm^{-2}$ remains stable for 500 h. Moreover, oxygen vacancies present in Ru-RSZ further reinforce the *d*–*d* interactions of Ru–Zr, contributing to the catalyst's activity and stability. This work provides an effective strategy for developing high-efficient and low-cost electrocatalysts for industrial hydrogen production.

Results and Discussion

Material Design and Theoretical Calculation

To validate the feasibility of the design strategy, DFT calculations were conducted to systematically compare the electronic structure and stability of the ZrO_2-supported Ru catalyst (denoted as Ru-RSZ) and commercial RuO_2 (Fig. 1a). Quantitative analysis of the intermetallic interactions provides direct evidence for the support stabilization effect: the integrated crystal orbital Hamilton population (ICOHP) for the Ru–Zr pair in Ru-RSZ is –0.001 eV, indicating a weak net bonding interaction.[15] In contrast, the ICOHP for the Ru–Ru pair in RuO_2 is +0.048 eV revealing a net antibonding interaction. Similarly, when Zr occupies the Ru sites in RuO_2 with D_{2h} symmetry, a net antibonding interaction (ICOHP = +0.021 eV) is also observed (Fig. S1). The direct *d*–*d* interaction between Zr and Ru not only reinforces the lattice framework but also markedly alters the 4*d* orbital distribution at Ru sites (Fig. 1b). Projected density of states (PDOS) and electronic band structure analyses (Fig. 1c, Fig. S2) reveal that the *d*-band center of the Ru 4*d* orbitals in Ru-RSZ shifts downward and farther from the Fermi level compared to that in com-RuO_2.[22] This modulation in electronic structure suggests a weakened adsorption strength for oxygen evolution reaction intermediates, which is anticipated to mitigate the catalytic activity limitation inherent to conventional RuO_2 caused by the over-binding of intermediates, thereby enhancing the intrinsic activity.[28] Furthermore, the altered coordination environment induces a further separation between the Ru 4*d* and O 2*p* bands, characterized by a downward shift of both band centers, resulting in an enlarged characteristic band gap ($\varepsilon_{d\text{-}p}$) of 2.91 eV for Ru-RSZ compared to 2.84 eV for RuO_2. This enlarged band gap indicates a reduced degree of covalent hybridization in the Ru–O bonds within Ru-RSZ, an electronic feature that contributes to suppressing the over-oxidation and dissolution of ruthenium under operational conditions, thereby enhancing the electrochemical stability of the catalyst.[29] The obviously increased Ru vacancy formation energy (Fig. 1d) in Ru-RSZ further corroborates, from a thermodynamic perspective, the superior stabilization effect exerted by the ZrO_2 support on the ruthenium active sites.[20,30]

Material Characterization and Coordination Environment

Ru-RSZ was synthesized via the co-precipitation method (Fig. S3). The resulting precipitate was then subjected to hydrothermal treatment at 200°C for 12 hours, followed by centrifugation and drying to obtain Ru-RSZ powder. XRD pattern affirms the presence of a tetragonal ZrO_2 phase (JCPDS 01-070-7300) in Ru-RSZ (Fig. 2a). No detectable peaks corresponding to Ru were observed, indicating that the lattice structure of ZrO_2 remains intact after Ru introduction (Fig. S4).[31] Notably, the XRD pattern of Ru-RSZ shifts slightly to higher diffraction angles compared to that of ZrO_2 (Fig. S5), indicating a decrease in the Ru-RSZ lattice constant owing to a smaller Ru atomic radius.[32] After the introduction of Ru, the peaks associated with the monoclinic phase of ZrO_2 were no longer detected, suggesting that Ru promotes the stabilization of the tetragonal phase. Raman spectroscopy (Fig. S6) confirmed the presence of the tetragonal ZrO_2 phase (t-ZrO_2) in the Ru-RSZ sample, with characteristic peaks at 284, 457 and 645 cm^{-1}.[33,34] No peaks from the monoclinic phase were observed. This result was accordance with the above XRD results. Furthermore, two Raman bands corresponded to tetragonal phase over Ru-RSZ sample were blue-shifted, suggesting a strong metal-support interaction between Ru and ZrO_2.[35,36]

To investigate the morphology and distribution of Ru atoms in Ru-RSZ, scanning electron microscopy (SEM) and spherical aberration-corrected HAADF-STEM image (Fig. 2b) were performed.[37] SEM and STEM images of Ru-RSZ reveal a morphology similar to that of ZrO_2, with both materials consisting of nanoparticles approximately 8 nm in diameter. (Fig. S7). The Z-contrast image acquired in HAADF-STEM (Fig. 2b), its Fast Fourier Transform (FFT) (inset) and the corresponding Z-contrast intensity profile show Ru (highlighted) randomly dispersed on Zr lattice sites in ZrO_2 projected along the [210] crystallographic direction. STEM-energy-dispersive spectroscopy (STEM-EDS) mapping (Fig. 2c, Fig. S8, Table S1) indicates uniform distribution of Ru, Zr, and O in Ru-RSZ with no obvious segregation (Ru atom percentage of metallic elements in Ru-RSZ is ≈10.8 at%).

The electronic structure of Ru-RSZ was further characterized by using X-ray photoelectron spectroscopy (XPS) and XAS. The full XPS spectrum of Ru-RSZ, RuO_2 and ZrO_2 is presented in Fig. S9. X-ray absorption near-edge spectroscopy (XANES) of Ru K-edge reveals a shift of the absorption edge to lower energy in Ru-RSZ compared to RuO_2, suggesting a decrease in the Ru valence state (Fig. 2d). The Zr K-edge XANES spectra indicate a near-edge absorption energy slightly higher than that of ZrO_2 (Fig. 2e). The Zr 3*d* XPS spectrum (Fig. S10) of Ru-RSZ exhibits a

View Article Online
DOI: 10.1039/D6SC01575A

discernible binding energy upshift of approximately 0.14 eV and 0.2 eV for the Zr $3d_{5/2}$ and Zr $3d_{3/2}$ peaks, respectively, compared to ZrO_2, suggesting a relatively higher oxidation state of Zr in Ru-RSZ, which agrees well with the XANES analysis results.[38,39] Meanwhile, the deconvolution of the Ru 3*p* XPS spectrum (Fig. S11, Table S2) indicates that the proportion of Ru^{III} in Ru-RSZ is 74%, significantly higher than that in RuO_2 (26%).[40] This higher ratio suggests electron transfer from the ZrO_2 support to Ru, leading to a reorganization of its local electronic structure, a conclusion further supported by the distinct negative shift in the Ru 3*p* binding energy peaks. The pre-reduction effect of Zr on Ru can effectively prevent the excessive oxidative dissolution of Ru during the OER process, thereby enhancing its stability.[41]

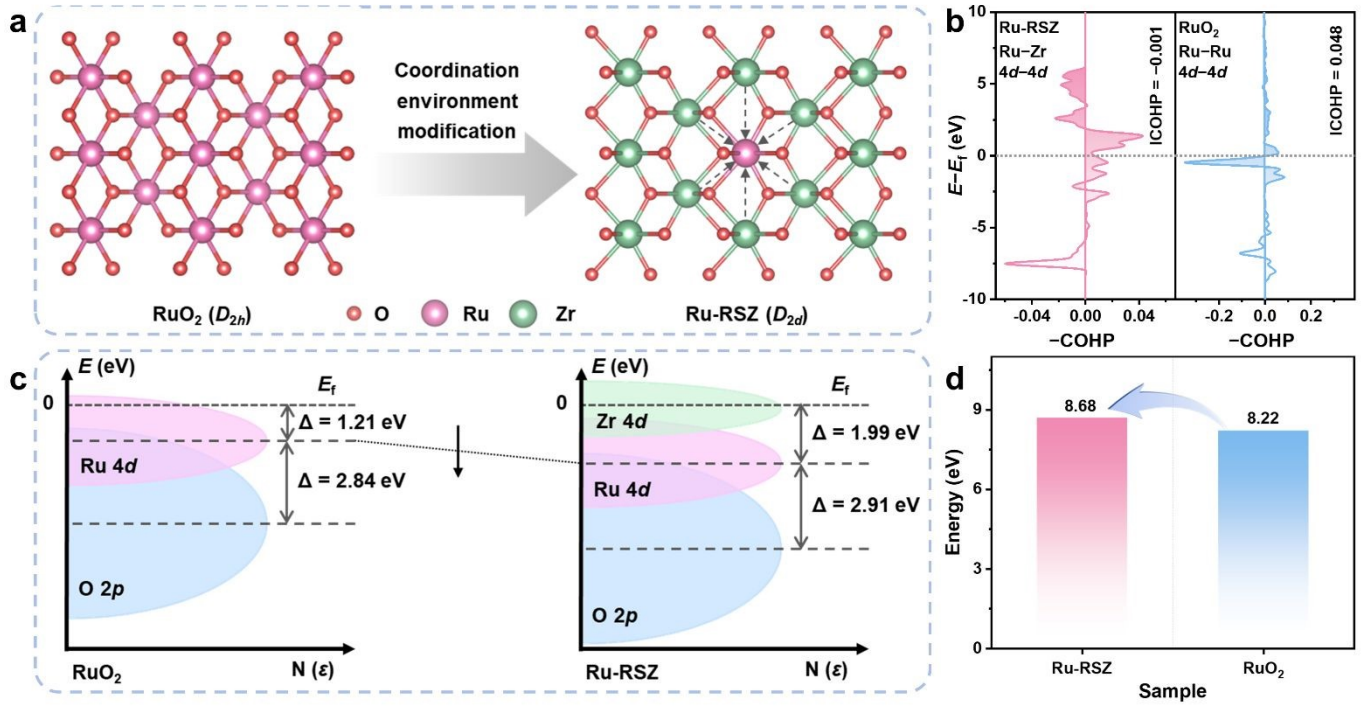

Fig. 1. (a) Schematic diagram of the design strategy for modifying the coordination environment of Ru. (b) Calculated COHP of Ru-RSZ and RuO_2. (c) Schematic diagram of band structure for Ru-RSZ and ZrO_2. (d) Ru vacancy formation energy of Ru-RSZ and RuO_2.

Wavelet Transform Extended X-ray Absorption Fine Structure (WT-EXAFS) indicates that the coordination environment of Ru in Ru-RSZ is the same as the Zr sites in ZrO_2 (featuring two Ru/Zr–O coordinations),[20] distinct from that in RuO_2 (which exhibits Ru–O and Ru–Ru coordinations) (Fig. 2f). Concurrently, Ru K-edge EXAFS reveals Ru–O and Ru–Ru/Zr scattering peaks in Ru-RSZ at approximately 1.6 Å, 2.8 Å, and 3.2 Å. Zr K-edge EXAFS likewise shows Zr–O and Zr–Zr scattering peaks in Ru-RSZ at 1.6 Å, 2.7 Å, and 3.2 Å, demonstrating that Ru and Zr occupy the same metal sites in the Ru/Zr oxide phase, with a symmetry change from D_{2h} to D_{2d} (Fig. 2g, Fig. S12, Fig. S13). In addition, EXAFS fitting results (Fig. 2h, Table S3) indicate a Ru–O coordination number of 7.4 in Ru-RSZ, evidencing a significant presence of oxygen vacancies.[16] Furthermore, the O 1*s* peak (Fig. S14) of Ru-RSZ is deconvoluted into three peaks at 529.6, 530.7, and 532.7 eV, corresponding to the lattice oxygen (O_L), surface oxygen vacancies (O_V) and surface oxygen adsorbates (O_{ads}), respectively.[42,43] The peak fitting results of the O 1*s* XPS spectra (Table S4) indicate that the proportion of oxygen vacancies in Ru-RSZ is 43%, significantly higher than the 29% observed in ZrO_2, suggesting a significant increase after Ru introduction. This finding is further corroborated by electron paramagnetic resonance (EPR) measurements (Fig. S15), which reveal a characteristic signal at g = 2.005 for Ru-RSZ (Fig. S15), corresponding to unpaired electrons trapped at oxygen vacancies, in good agreement with the XPS O 1s analysis.[29]

Electrochemical Performance in Acidic Electrolytes

The OER performance of Ru-RSZ, ZrO_2 and RuO_2 catalysts were evaluated in a three-electrode system using 0.5 M H_2SO_4 as the electrolyte. Linear sweep voltammetry (LSV) and corresponding Tafel analysis (Fig. 3a, Fig. 3b) demonstrated that the Ru-RSZ catalyst exhibits outstanding electrocatalytic activity, requiring an overpotential (η) of only 208 mV to achieve a current density of 10 mA·cm^{-2} along with a Tafel slope of 62.15 mV·dec^{-1}. These values are substantially lower than those of a value substantially lower than those of RuO_2 (265 mV and 71.97 mV·dec^{-1}), while the ZrO_2 support showed negligible OER activity. Notably, the Ru specific mass activity (Fig. 3c, Fig. S16) of the Ru-RSZ catalyst was calculated to be as high as 1,452.61 A·g_{Ru}^{-1} at η = 1.51 V, which is more than 40.1 times higher than that of RuO_2 (36.21 A·g_{Ru}^{-1} at 1.51 V). To further evaluate the intrinsic activity of the Ru species, the turnover frequency (TOF) was calculated and plotted against the overpotential (Fig. S17). The calculated TOF value for Ru-RSZ reached 0.38 s^{-1} at an overpotential of 1.51 V, representing a 38-fold enhancement over that of RuO_2 (0.01 s^{-1}). Double-layer capacitance (C_{dl}) was measured to determine the electrochemical active surface area (ECSA) for evaluating

View Article Online
DOI: 10.1039/D5SC05751A

the OER performance (Fig. 3d, Fig. S18, Table S5). Ru-RSZ demonstrates the highest C_{dl} of 13.67 mF · cm^{-2} and ECSA (390.57 cm^2), values approximately 1.43 times greater than those of RuO_2 (9.56 mF·cm^{-2} and 273.14 cm^2). This indicates a significantly increased number of available active sites in Ru-RSZ, which effectively enhances its OER performance. Additionally, the OER activity normalized to the electrochemical surface area of Ru-RSZ and RuO_2 was also calculated (Fig. S19). The ECSA-normalized mass activity of Ru-RSZ reached 0.16 mA·cm^{-2} at 1.51 V (vs. RHE), which is 3.2 times higher than that of RuO_2 (0.05 mA · cm^{-2}) and further demonstrating its superior intrinsic OER catalytic activity.

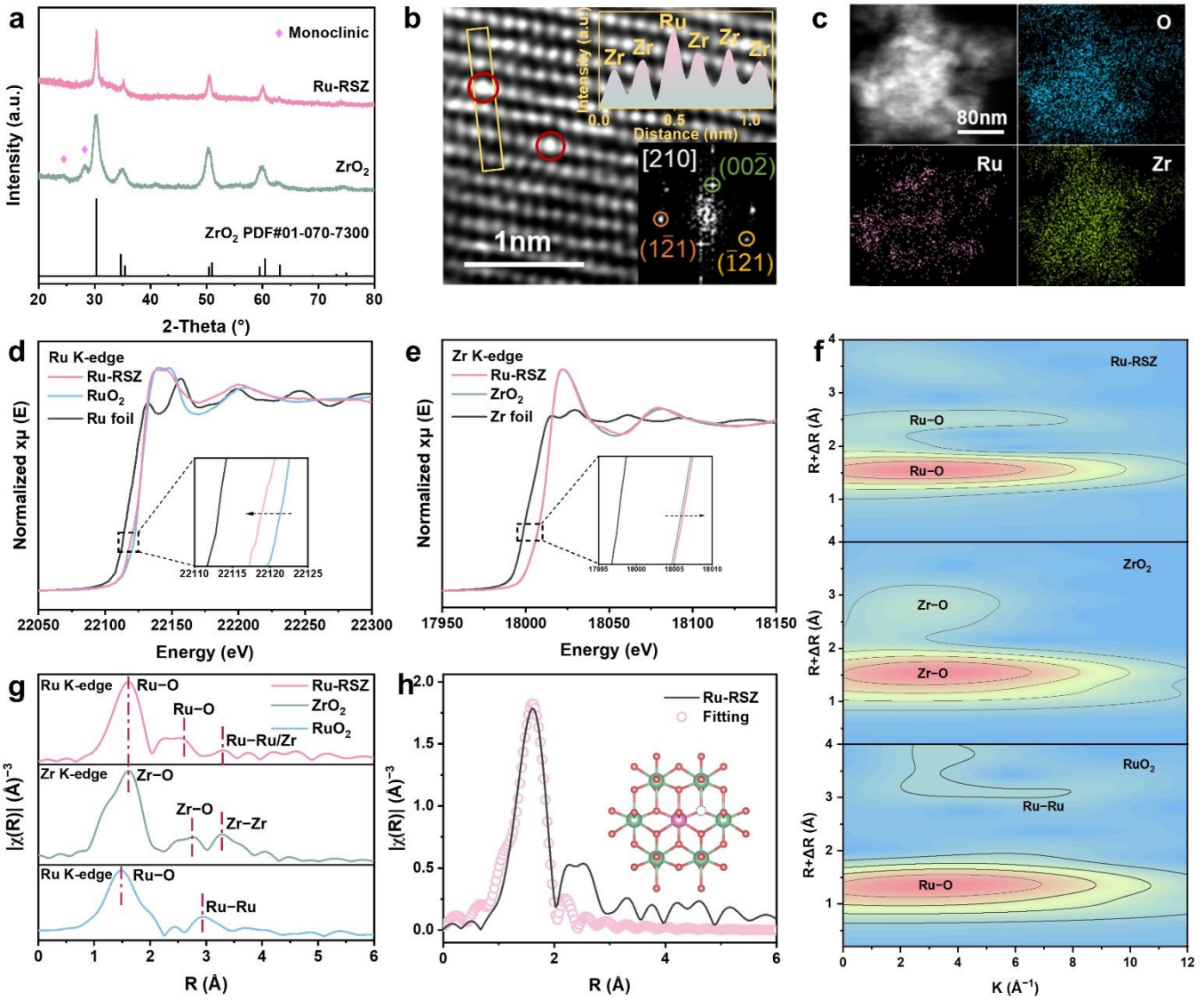

Fig. 2. (a) XRD patterns of Ru-RSZ and ZrO_2. (b) HAADF-STEM and corresponding FFT image (inset) of Ru-RSZ along [210] orientation with Z-contrast intensity line profile extracted from the marked area. The bright spots highlighted by red circles correspond to isolated Ru atoms occupying Zr lattice sites. (c) HAADF-STEM image corresponding EDS maps of Ru-RSZ. (d) Normalized Ru K-edge XANES spectra of Ru-RSZ, RuO_2, and Ru foil. (e) Normalized Zr K-edge XANES spectra of Ru-RSZ, ZrO_2 and Zr foil. (f) Wavelet-transformed of k^3-weighted EXAFS signals of RSZ, ZrO_2 and RuO_2. (g) Fourier transform R-space of the experimental EXAFS signal collected at the Ru K-edge for Ru-RSZ and RuO_2, and Zr K-edge for ZrO_2. (h) R-space fitting results of Ru K-edge XAFS spectra for Ru-RSZ.

Electrochemical impedance spectroscopy (EIS) is a powerful technique to examine the electrical charge transfer behavior across interfaces and phases in electrochemical systems.[44] The EIS measurements (Fig. 3e) revealed well-defined semicircular Nyquist plots for Ru-RSZ, RuO_2, and ZrO_2.[45] Among these, Ru-RSZ exhibited a semicircle with a notably smaller radius compared to RuO_2 and ZrO_2. The fitting results (Table S6) indicated a significantly lower charge-transfer resistance (R_{ct}) and more efficient electron transfer across the electrode/electrolyte interface. The stability of Ru-RSZ was evaluated by chronopotentiometry (CP) at a constant current density of 10 mA·cm^{-2} (Fig. 3f). Compared to the commercial RuO_2 catalyst, Ru-RSZ exhibited excellent stability, maintaining most of its potential over a 500-hour period, with some cases even showing a slight performance enhancement as indicated aby a decrease in overpotential. Post-reaction characterization (Fig. S20) confirmed that the crystal structure and atomic dispersion of Ru remained intact, further supporting the structural robustness of the catalyst. The OER performance of Ru-RSZ outperformed RuO_2 across all five considered

View Article Online
DOI: 10.1039/D6SC01575A

dimensions (Fig. 3g and Table S7). The outstanding activity and stability of Ru-RSZ significantly exceed those of previously reported noble metal electrocatalysts in acidic electrolytes (Fig. 3h, Table S8).

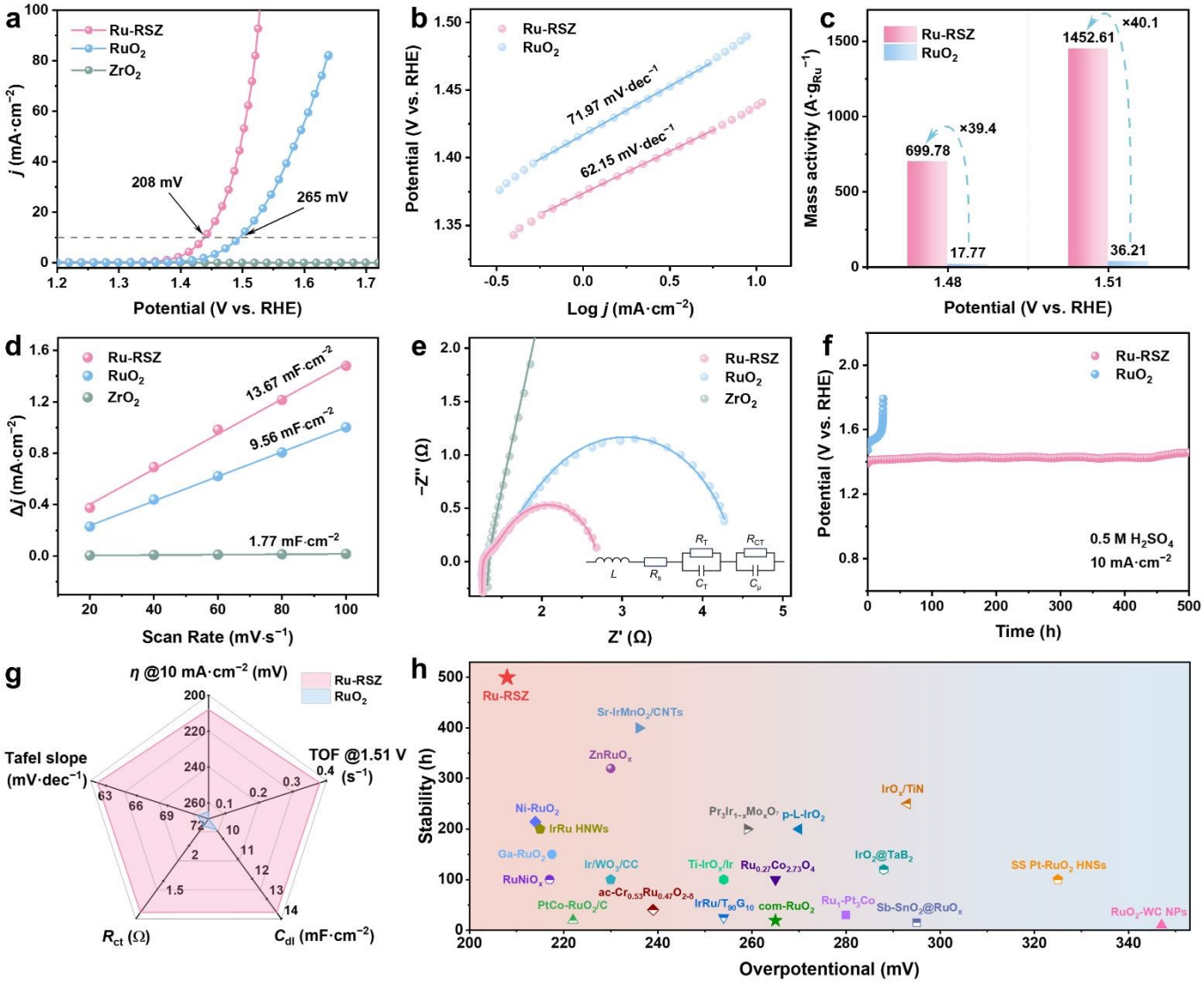

Fig. 3. Electrocatalytic OER performance evaluation in 0.5 M H_2SO_4 electrolyte. (a) LSV polarization curves and (b) Tafel plots of Ru-RSZ and RuO_2. (c) Ru mass activities of Ru-RSZ and RuO_2 at 1.48 and 1.51 V vs. RHE. (d) C_{dl} plots and (e) Nyquist plots of Ru-RSZ, ZrO_2 and RuO_2 derived from CV curves. (f) Chronopotentiometry test at 10 mA·cm^{-2} of electrocatalysts. (g) Summary of some major OER performance metrics of Ru-RSZ and RuO_2. (h) Comparison of the overpotential and stability of Ru-RSZ with previously reported OER electrocatalysts in acidic electrolyte.

Insights into the OER catalytic mechanism

To elucidate the regulatory mechanism of oxygen vacancies on the electronic structure of catalytic sites, systematic DFT calculations were conducted on Ru-RSZ-O_V, Ru-RSZ, and RuO_2. Structural optimization (Fig. 4a) reveals that the formation of an oxygen vacancies induces notable local structural relaxation, reducing the distance between Ru and the adjacent Zr atom from 3.98 Å (Ru-RSZ) to 2.87 Å (Ru-RSZ-O_V), thereby creating favorable geometric conditions for interatomic orbital interactions.[22] Charge density difference and Bader charge analyses (Fig. 4b, Table S9) collectively unveil the charge redistribution triggered by the oxygen vacancies, with pronounced electron accumulation observed in the Ru–Zr bridging region, preliminarily indicating enhanced *d*–*d* orbital interaction.[46] The Bader charge on the Ru atom in Ru-RSZ-O_V decreases to +0.3099 |e|, lower than its value of +0.8249 |e| in Ru-RSZ, while the charge on the adjacent Zr atom also decreases from +1.6345|e| to +1.5131|e|, suggesting weakened electron localization and enhanced covalency.[47] Notably, the Bader charge of Ru in Ru-RSZ-O_V is lower than that of Ru in RuO_2 (+1.4893 |e|), while the charge of its Zr is higher than that of Zr in ZrO_2 (+1.2822 |e|), providing clear evidence for electron transfer from Zr to Ru, aligning with the valence state trend measured by XAS, jointly confirming the metal-support electronic synergy.

In-depth analysis of the electronic structure shows that the PDOS (Fig. 4c) of the Ru-4*d* and Zr-4*d* orbitals in Ru-RSZ-O_V exhibit significantly enhanced peak overlap and hybridization near the Fermi level, confirming the effective promotion of *d*–*d* orbital coupling between Ru and Zr by the oxygen vacancies.[48]

View Article Online
DOI: 10.1039/D5SC05754J

Furthermore, the separation between their *d*-band centers contracts from 1.77 eV in Ru-RSZ to 1.30 eV in Ru-RSZ-Ov, implying a reduced average energy difference and closer spatial distribution between the Ru-4*d* and Zr-4*d* orbitals, which further supports the conclusion of enhanced *d*–*d* orbital coupling. This coupling drives electron transfer from Zr to Ru, resulting in a moderate upshift of the Ru *d*-band center (from −1.99 eV to −1.72 eV) and a concomitant downshift of the Zr *d*-band center (from −0.42 eV to −0.22 eV) in Ru-RSZ-O_V, a theoretically calculated charge redistribution that is consistent with the XAS analysis. The moderate upshift of the Ru *d*-band center facilitates the optimization of its adsorption free energy for OER intermediates, thereby enhancing the intrinsic activity.[49] Concurrently, its energy level remains substantially lower than that of RuO_2 (−1.21 eV), which is beneficial for suppressing the over-oxidation of Ru and consequently improving the electrochemical stability.

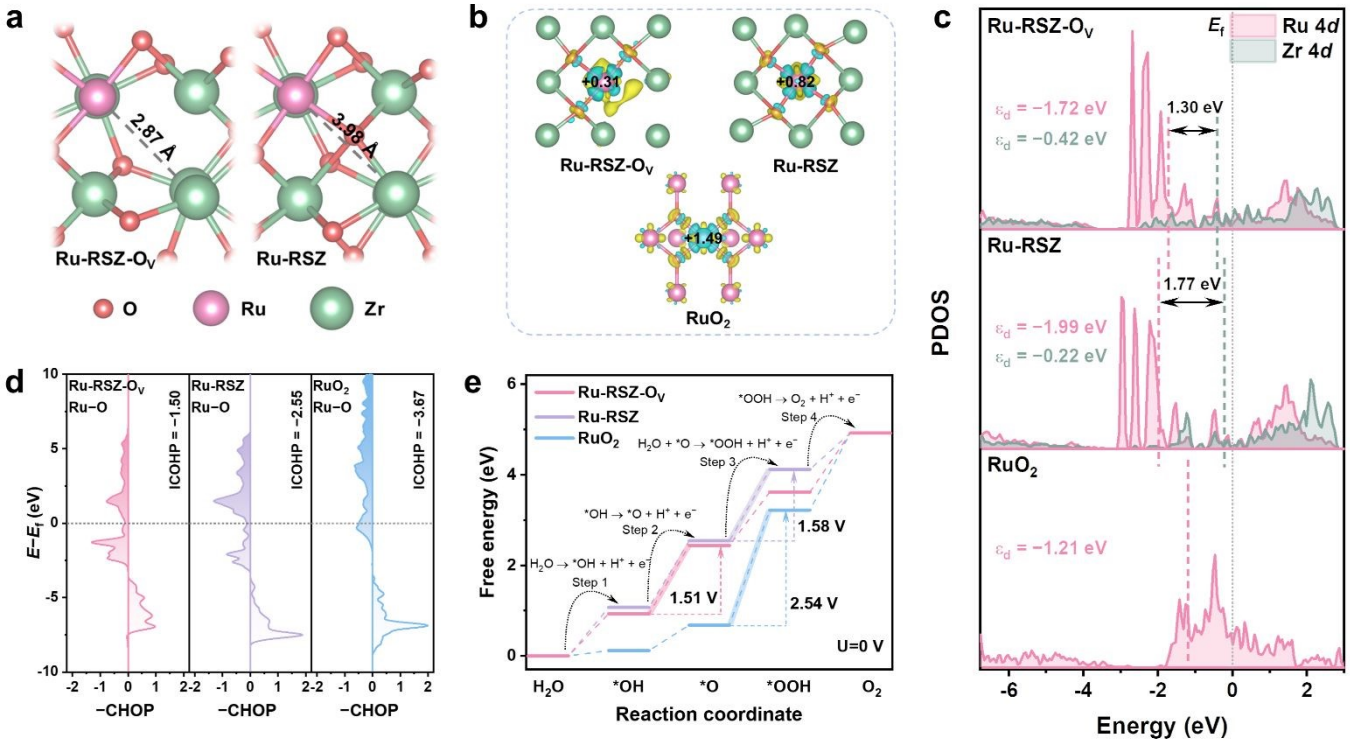

Fig. 4. Theoretical simulation and analysis. (a) Comparison of Ru-Zr atomic distances in Ru-RSZ-O_V (left) and Ru-RSZ (right). (b) Differential charge density and Bader charge calculation of Ru-RSZ-O_V, Ru-RSZ and RuO_2 (yellow indicates charge accumulation, while blue indicates charge depletion). (c) The PDOS of Ru 4*d* and Zr 4*d* for Ru-RSZ-O_V, Ru-RSZ and RuO_2. (d) Calculated COHP of Ru-RSZ-O_V, Ru-RSZ and RuO_2. (e) Gibbs free energy diagrams via the AEM pathway on Ru site at U = 0 V for Ru-RSZ-O_V, Ru-RSZ and RuO_2.

Direct evidence for chemical bond strengthening is provided by ICOHP analysis. The ICOHP value for the Ru–Zr atomic pair (Fig. S21) decreases significantly from −0.001 eV in Ru-RSZ to −0.089 eV in Ru-RSZ-O_V, demonstrating a significant enhancement of the Ru–Zr bond induced by the oxygen vacancies. Simultaneously, analysis of the Ru site reveals that the ICOHP value (Fig. 5d) for the Ru–O bond in Ru-RSZ-Ov exhibits a less negative value (−1.50 eV) compared to those in Ru-RSZ (−2.55 eV) and RuO_2 (−3.067 eV), indicating a weakened covalent character. This attenuation is attributed to the Ru—Zr *d*–*d* orbital coupling, which effectively modulates the adsorption strength of oxygenated intermediates on the Ru active sites, thereby optimizing the reaction kinetics of the OER. Furthermore, pH-dependent and tetramethylammonium cation (TMA^+) probing measurements were further used to demonstrate the restricted lattice oxygen activity in Ru-RSZ (Figs. S22-24). According to the calculated proton reaction orders (ρ = ∂log(j)/ ∂pH), RuO_2 shows significant pH-dependent (ρ=-0.165) OER activity, whereas Ru-RSZ reflects a pH-independent (ρ=-0.076) characteristic in which the current density nearly remains constant as the pH value changes. This result indicates that the degree of non-equilibrium proton-electron coupling transfer of Ru-RSZ has decreased.[23] Moreover, the addition of TMA^+ in 0.5M H_2SO_4 does not affect the OER activity of Ru-RSZ, whereas a clear inhibition is observed for RuO_2, indicating the amount of *OO intermediates produced by Ru-RSZ is lower, demonstrating that the extent of lattice oxygen involvement in the OER process is reduced and the stability of lattice structure has been optimized.[50] Gibbs free energy calculations (Fig. 5e, Fig. S25, Fig. S26) demonstrate that the adsorption energies of Ru-RSZ-O_V for all OER intermediates lies between those of Ru-RSZ and RuO_2, achieving a more balanced adsorption strength.[51] Concurrently, rate-determining step (RDS) energy barrier for Ru-RSZ-Ov is the lowest (1.51 eV，$^*OH \rightarrow {}^*O + H^+ + e^-$) among the studied catalysts, being lower than those for Ru-RSZ (1.58 eV，$H_2O + {}^*O \rightarrow {}^*OOH + H^+ + e^-$) and RuO_2 (2.41 eV). The change in the RDS coupled with the significant reduction in the energy barrier collectively contributes to the enhanced OER activity.[30] The vacancy formation energy calculations (Fig. S27) indicate that the Ru vacancy formation energy in Ru-RSZ-O_V (8.94 eV) is higher than those in RuO_2 (8.22 eV) and Ru-RSZ (8.68 eV), suggesting greater resistance of the Ru species to dissolution, which further corroborates, from a thermodynamic perspective, the crucial role of *d*–*d* orbital coupling in enhancing OER stability.

View Article Online
DOI: 10.1039/D6SC01575A

ARTICLE

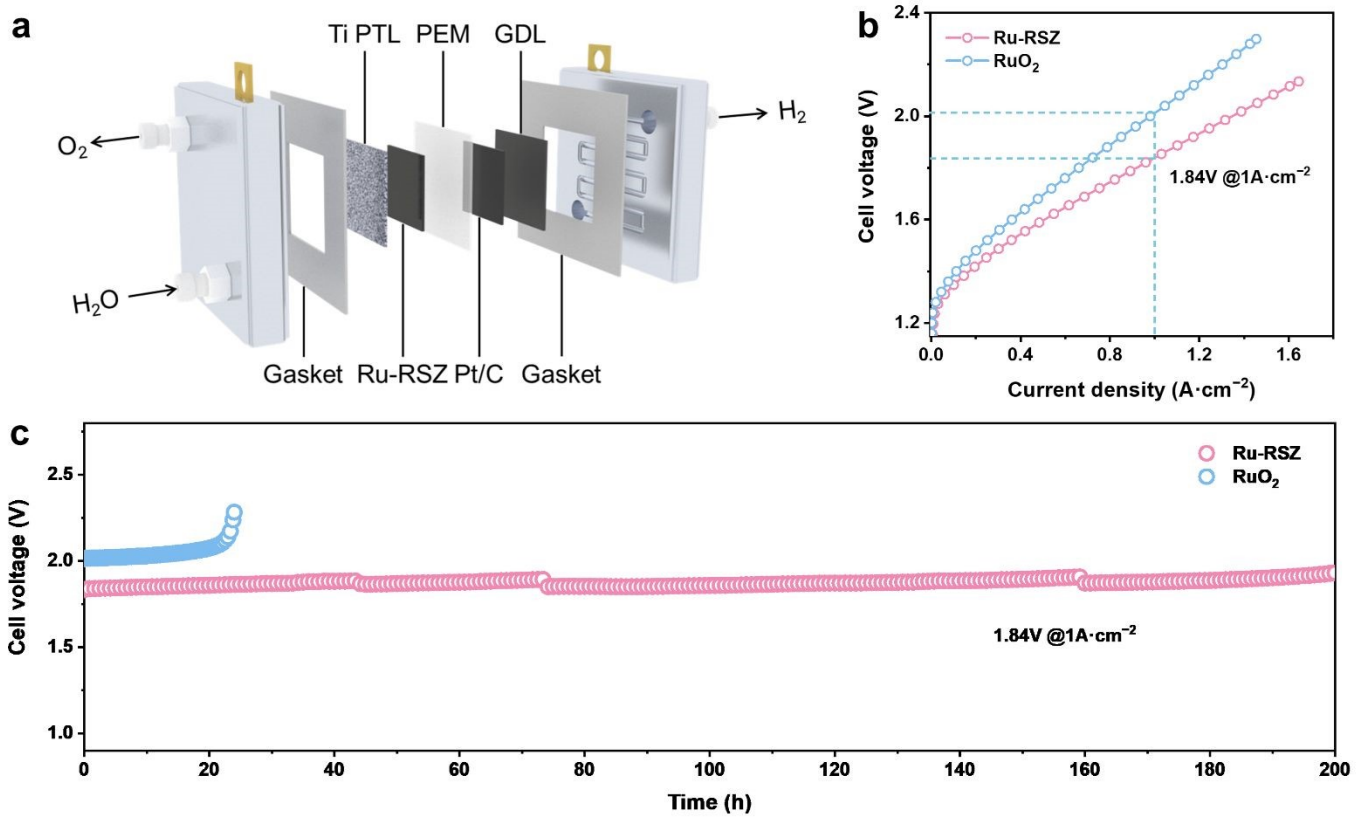

Fig. 5. (a) Schematic diagram of the PEM electrolyzer using Ru-RSZ as anode electrocatalyst. (b) Polarization curves of PEMWE employing Ru-RSZ and RuO_2 as the anodic electrocatalyst. (c) Chronopotentiometry curve of Ru-RSZ and RuO_2 in a PEMWE electrolyzer at 1 A·cm^{-2}.

PEMWE Performance Evaluation

To further verify the performance of Ru-RSZ for practical applications in water electrolysis, a membrane electrode assembly was constructed utilizing a Nafion 211 membrane with Ru-RSZ as the anode catalyst and commercial Pt/C as the cathode catalyst, respectively (Fig. 5a). The mass loading of Ru in anode of the PEMWE tests is 175.7 $\mu g_{Ru} \cdot cm^{-2}$. The polarization curve (without *iR* compensation) confirms the superior catalytic activity of Ru-RSZ compared to commercial RuO_2. Specifically, the Ru-RSZ-based PEMWE electrolyzer to deliver a current density of 1 A·cm^{-2} at a cell voltage of 1.84 V, which is 180 mV lower than the voltage required by commercial RuO_2 (Fig. 5b).[11,52] Furthermore, the long-term stability of the PEMWE with the Ru-RSZ anode was evaluated by CP test at a constant current density of 1 $A \cdot cm^{-2}$ (Fig. 5c). The result indicates that the cell voltage of the remained stable throughout the 200-hour test period, with no significant increase observed. These results strongly confirm that the electronic regulation of Ru by the ZrO_2 support could enhance both the catalytic activity and stability of Ru-RSZ, demonstrating significant potential for practical application in PEMWE.

Conclusions

In summary, this work culminates in the synthesis of a Ru electrocatalyst anchored on a zirconia support (Ru-RSZ), wherein the electronic structure of the Ru active sites is precisely modulated through the establishment of Ru–Zr 4*d*–4*d* coupling via oxygen vacancy generation, leading to substantially improved activity and stability for the acidic OER. The successful stabilization of the tetragonal ZrO_2 phase upon Ru incorporation was confirmed by XRD and Raman spectroscopy, while the formation of oxygen vacancies induced by Ru doping was evidenced by XAS and XPS analyses. DFT calculations provide a mechanistic foundation, showing that the coupling redistributes electron density and weakens the binding strength of oxygen intermediates, thereby optimizing the reaction

kinetics. The optimized Ru-RSZ electrode delivers a low overpotential of 208 mV at 10 mA cm^{-2} and a mass activity (1452.61 $A \cdot g_{Ru}^{-1}$ @ 1.51 V) 40.1 times greater than that of commercial RuO_2. Its practical viability is further demonstrated in a PEMWE cell, achieving 1.84 V at 1 A cm^{-2} with stable operation for >200 h. Consequently, this work presents a rational and effective strategy for the development of efficient and durable Ru-based electrocatalysts for practical renewable energy conversion technologies.

Author contributions

D. Yu conceived the project, performed all the electrochemical measurements, and wrote the initial draft of the manuscript. H. Zhao and Y. Zhang reviewed and edited the manuscript. B. Liu, D. Li, and J. Yu provided useful discussions and insights. X. Li and S. Liu contributed to the interpretation of the experimental results. Z. Li and P. Gao supervised the research. All authors contributed to the manuscript.

Conflicts of interest

The authors declare no competing financial interest.

Data availability

The data supporting the findings of this article are available within the paper and the SI.

Acknowledgements

This work was financially supported by the National Natural Science Foundation of China (22478450), Sichuan Province Science and Technology Education Joint Fund Project (2025NSFSC2057), Liaoning Binhai Laboratory Project (LBLF-202306) and the Science and Technology Foundation of Dalian City (2022JJ11CG005).

Notes and references

1 H. Jun, E. Kang, J. Moon, H. Kim, S. Han, S. Choung, S. Kim, S. Y. Yi, E. Kang, C. H. Choi, J. W. Han and J. Lee, *Chem*, 2025, **11**, 102367.
2 Y. Jiao, Y. Zheng, M. Jaroniec and S. Z. Qiao, *Chem. Soc. Rev.*, 2015, **44**, 2060-2086.
3 X. Wang, Z. Li, H. Jang, C. Chen, S. Liu, L. Wang, M. G. Kim, J. Cho, Q. Qin and X. Liu, *Adv. Energy Mater.*, 2024, **15**, 2403388.
4 S. Yang, Q. Shu, B. Fu, S. Liu, Y. Zhang and H. Zhao, *Chem. Eng. J.*, 2024, **488**, 150905.
5 R.-T. Liu, Z.-L. Xu, F.-M. Li, F.-Y. Chen, J.-Y. Yu, Y. Yan, Y. Chen and B. Y. Xia, *Chem. Soc. Rev.*, 2023, **52**, 5652-5683.
6 C.-Z. Yuan, S. Wang, K. San Hui, K. Wang, J. Li, H. Gao, C. Zha, X. Zhang, D. A. Dinh, X.-L. Wu, Z. Tang, J. Wan, Z. Shao and K. N. Hui, *ACS Catal.*, 2023, **13**, 2462-2471.
7 R. Ram, L. Xia, H. Benzidi, A. Guha, V. Golovanova, A. Garzon Manjon, D. Llorens Rauret, P. Sanz Berman, M. Dimitropoulos, B. Mundet, E. Pastor, V. Celorrio, C. A. Mesa, A. M. Das, A. Pinilla-Sanchez, S. Gimenez, J. Arbiol, N. Lopez and F. P. Garcia de Arquer, *Science*, 2024, **384**, 1373-1380.
8 Z.-P. Wu, H. Zhang, S. Zuo, Y. Wang, S. L. Zhang, J. Zhang, S.-Q. Zang and X. W. Lou, *Adv. Mater.*, 2021, **33**, 2103004.
9 J. Chen, J. Ma, T. Huang, Q. Liu, X. Liu, R. Luo, J. Xu, X. Wang, T. Jiang, H. Liu, Z. Lv, T. Yao, G. Wang, X. Zheng, Z. Li and W. Chen, *Angew. Chem., Int. Ed.*, 2025, **64**, e202503330.
10 J. Park, D. W. Lee, J. Hyun, H. Lee, E. Oh, K. Seok, G. Doo and H.-T. Kim, *Energy Environ. Sci.*, 2025, **18**, 5577-5585.
11 W. He, X. Tan, Y. Guo, Y. Xiao, H. Cui and C. Wang, *Angew. Chem., Int. Ed. Engl.*, 2024, **63**, e202405798.
12 M. Zhang, W. An, Q. Liu, Y. Jiang, X. Zhao, H. Chen, Y. Zou, X. Liang and X. Zou, *Nat. Commun.*, 2025, **16**, 7608.
13 J. Chen, Y. Ma, T. Huang, T. Jiang, S. Park, J. Xu, X. Wang, Q. Peng, S. Liu, G. Wang and W. Chen, *Adv. Mater.*, 2024, **36**, e2312369.
14 G. Chen, R. Lu, C. Ma, X. Zhang, Z. Wang, Y. Xiong and Y. Han, *Angew. Chem., Int. Ed. Engl.*, 2024, **63**, e202411603.
15 L. Li, G. Zhang, C. Zhou, F. Lv, Y. Tan, Y. Han, H. Luo, D. Wang, Y. Liu, C. Shang, L. Zeng, Q. Huang, R. Zeng, N. Ye, M. Luo and S. Guo, *Nat. Commun.*, 2024, **15**, 4974.
16 Y. Shen, X.-L. Zhang, M.-R. Qu, J. Ma, S. Zhu, Y.-L. Min, M.-R. Gao and S.-H. Yu, *Nat. Commun.*, 2024, **15**, 7861.
17 J. Chen, Y. Ma, C. Cheng, T. Huang, R. Luo, J. Xu, X. Wang, T. Jiang, H. Liu, S. Liu, T. Huang, L. Zhang and W. Chen, *J. Am. Chem. Soc.*, 2025, **147**, 8720-8731.
18 J. Zhang, H. Qin, X. Cao, W. Jia, R. Ma, X. Chen, W. Xia, G. Lin and L. Jiao, *ACS Mater. Lett.*, 2024, **6**, 3016-3024.
19 Y. Qin, S. Deng, X.-Y. Zhou, Z. Yan, L. He, K. Li and T.-Y. Zhang, *J. Am. Chem. Soc.*, 2025, **147**, 30943-30955.
20 L. Deng, H. Chen, S.-F. Hung, Y. Zhang, H. Yu, H.-Y. Chen, L. Li and S. Peng, *J. Am. Chem. Soc.*, 2024, **146**, 35438-35448.
21 X. Li, H. Rong, J. Zhang, D. Wang and Y. Li, *Nano Res.*, 2020, **13**, 1842-1855.
22 C. Zhou, L. Li, Z. Dong, F. Lv, H. Guo, K. Wang, M. Li, Z. Qian, N. Ye, Z. Lin, M. Luo and S. Guo, *Nat. Commun.*, 2024, **15**, 9774.
23 X. Zhang, Y. Zhang, B. O. Protsenko, M. A. Soldatov, J. Zhang, C. Yang, S. Bo, H. Wang, X. Chen, C. Wang, W. Cheng and Q. Liu, *Nat. Commun.*, 2025, **16**, 6921.
24 Y. Li, J. Zhao, S. Zhang, Y. Fan, C. Y. Kuo, Y. C. Ku, T. S. Chan, C. W. Kao, Y. C. Huang, C. T. Chen, S. C. Haw, C. Jin, H. Zhao, D. Ye, C. Jing, Z. Hu and L. Zhang, *J. Am. Chem. Soc.*, 2025, **147**, 26854-26864.
25 B.-J. Kim, D. F. Abbott, X. Cheng, E. Fabbri, M. Nachtegaal, F. Bozza, I. E. Castelli, D. Lebedev, R. Schäublin, C. Copéret, T. Graule, N. Marzari and T. J. Schmidt, *ACS Catal.*, 2017, **7**, 3245-3256.
26 Z.-Q. Jiang, C.-Z. Fan, J.-Y. Pan, L. Shao, H. Chen, E. Pervaiz, Y. Dong, T.-Z. Wang, X.-R. Zheng, J.-H. Li and Y.-D. Deng, *Rare Met.*, 2024, **43**, 2891-2912.
27 H. Yu, C. Wang, X. Xin, Y. Wei, S. Li, Y. An, F. Sun, T. Lin and L. Zhong, *Nat. Commun.*, 2024, **15**, 5143.
28 Y. Lin, Z. Tian, L. Zhang, J. Ma, Z. Jiang, B. J. Deibert, R. Ge and L. Chen, *Nat. Commun.*, 2019, **10**, 162.
29 F. Wang, L. Feng, M. Zhang and H. Cong, *Nat. Commun.*, 2025, **16**, 6624.
30 J. Zhang, L. Xu, X. Yang, S. Guo, Y. Zhang, Y. Zhao, G. Wu and G. Li, *Angew. Chem., Int. Ed.*, 2024, **63**, e202405641.
31 T. Wu, X. Zhu, Z. Xing, S. Mou, C. Li, Y. Qiao, Q. Liu, Y. Luo, X. Shi, Y. Zhang and X. Sun, *Angew. Chem., Int. Ed. Engl.*, 2019, **58**, 18449-18453.
32 W. Q. Zaman, W. Sun, M. Tariq, Z. Zhou, U. Farooq, Z. Abbas, L. Cao and J. Yang, *Appl. Catal., B*, 2019, **244**, 295-302.
33 M. C. Uribe López, M. A. Alvarez Lemus, M. C. Hidalgo, R. López González, P. Quintana Owen, S. Oros-Ruiz, S. A. Uribe López and J. Acosta, *J. Nanomater.*, 2019, **2019**, 1-12.
34 C. Li, Z. Han, Y. Hu, T. Liu and X. Pan, *RSC Adv.*, 2022, **12**, 27309-27320.

View Article Online
DOI: 10.1039/D6SC01575A

35 C. Dong, R. Mu, R. Li, J. Wang, T. Song, Z. Qu, Q. Fu and X. Bao, *J. Am. Chem. Soc.*, 2023, **145**, 17056-17065.
36 Z. Zhang, S. Lu, M. Zhu, F. Wang, K. Yang, B. Dong, Q. Yao and W. Hu, *J. Am. Chem. Soc.*, 2025, **147**, 22806-22817.
37 N. Zhang, Y. Hu, L. An, Q. Li, J. Yin, J. Li, R. Yang, M. Lu, S. Zhang, P. Xi and C. H. Yan, *Angew. Chem., Int. Ed. Engl.*, 2022, **61**, e202207217.
38 X. Fang, S. Wu, Y. Wu, W. Yang, Y. Li, J. He, P. Hong, M. Nie, C. Xie, Z. Wu, K. Zhang, L. Kong and J. Liu, *Appl. Surf. Sci.*, 2020, **518**, 146226.
39 M. Yang, X. Guan, Z. Shi, H. Wu, Y. Cheng, Z. Wang, W. Liu, F. Xiao, M. Shao, M. Xiao, C. Liu and W. Xing, *Small*, 2025, **22**, 2411117.
40 Z. Li, H. Sheng, Y. Lin, H. Hu, H. Sun, Y. Dong, X. Chen, L. Wei, Z. Tian, Q. Chen, J. Su and L. Chen, *Adv. Funct. Mater.*, 2024, **34**, 2409714.
41 J. Zhao, Y. Guo, Z. Zhang, X. Zhang, Q. Ji, H. Zhang, Z. Song, D. Liu, J. Zeng, C. Chuang, E. Zhang, Y. Wang, G. Hu, M. A. Mushtaq, W. Raza, X. Cai and F. Ciucci, *Nat. Nanotechnol.*, 2025, **20**, 57-66.
42 R. Deng, F. Liu, S. Gao, Z. Xia, R. Wu, J. Kong, J. Yang, J. Wen, X. Zhang, C. Lv, Y. Wang, X. Li and Z. Wang, *ACS Catal.*, 2025, **15**, 1782-1794.
43 Q. Yao, J. Le, S. Yang, J. Cheng, Q. Shao and X. Huang, *Chin. J. Catal.*, 2022, **43**, 1493-1501.
44 J. M. P. Martirez and E. A. Carter, *J. Am. Chem. Soc.*, 2019, **141**, 693-705.
45 S. Wang, Q. Jiang, S. Ju, C. S. Hsu, H. M. Chen, D. Zhang and F. Song, *Nat. Commun.*, 2022, **13**, 6650.
46 Q. Ji, B. Tang, X. Zhang, C. Wang, H. Tan, J. Zhao, R. Liu, M. Sun, H. Liu, C. Jiang, J. Zeng, X. Cai and W. Yan, *Nat. Commun.*, 2024, **15**, 8089.
47 Q. Qin, Z. Li, X. Zhao, H. Zhao, L. Zhai, M. Gyu Kim, J. Cho, H. Jang, S. Liu and X. Liu, *Angew. Chem., Int. Ed. Engl.*, 2025, **64**, e202413657.
48 H. Wang, T. Zhai, Y. Wu, T. Zhou, B. Zhou, C. Shang and Z. Guo, *Adv. Sci.*, 2023, **10**, 2301706.
49 Y. Qin, T. Yu, S. Deng, X.-Y. Zhou, D. Lin, Q. Zhang, Z. Jin, D. Zhang, Y.-B. He, H.-J. Qiu, L. He, F. Kang, K. Li and T.-Y. Zhang, *Nat. Commun.*, 2022, **13**, 3784.
50 K. Zhou, Y. Wang, Z. Jiang, B. Dai and Z. J. Jiang, *Adv. Mater.*, 2025, **37**, 2420159.
51 Y. Xu, Z. Mao, J. Zhang, J. Ji, Y. Zou, M. Dong, B. Fu, M. Hu, K. Zhang, Z. Chen, S. Chen, H. Yin, P. Liu and H. Zhao, *Angew. Chem., Int. Ed.*, 2024, **63**, e202316029.
52 Z.-Y. Wu, F.-Y. Chen, B. Li, S.-W. Yu, Y. Z. Finfrock, D. M. Meira, Q.-Q. Yan, P. Zhu, M.-X. Chen, T.-W. Song, Z. Yin, H.-W. Liang, S. Zhang, G. Wang and H. Wang, *Nat. Mater.*, 2023, **22**, 100-108.

View Article Online
DOI: 10.1039/D6SC01575A

Data availability statements

The data supporting the findings of this article are available within the paper and the SI.